



NOVA

University of Newcastle Research Online

nova.newcastle.edu.au

Linul, Emanoil; Lell, Daniel; Movahedi, Nima; Codrean, Cosmin; Fiedler, Thomas.  
“Compressive properties of zinc syntactic foams at elevated temperatures”. Published in  
*Composites Part B: Engineering* Vol. 167, p. 122-134 (2019).

**Available from:** <http://dx.doi.org/10.1016/j.compositesb.2018.12.019>

© 2019. This manuscript version is made available under the CC-BY-NC-ND 4.0 license  
<http://creativecommons.org/licenses/by-nc-nd/4.0/>

**Accessed from:** <http://hdl.handle.net/1959.13/1423357>

# Compressive properties of Zinc Syntactic Foams at elevated temperatures

Emanoil Linul<sup>1,\*</sup>, Daniel Lell<sup>2</sup>, Nima Movahedi<sup>2</sup>, Cosmin Codrean<sup>1</sup>, Thomas Fiedler<sup>2</sup>

<sup>1</sup>Politehnica University of Timisoara, Faculty of Mechanical Engineering, 1 Mihai Viteazu Avenue, 300 222 Timisoara, Romania

<sup>2</sup>The University of Newcastle, School of Engineering, NSW 2287 Callaghan, Australia

\*Corresponding author: Emanoil LINUL, E-mail: emanoil.linul@upt.ro.

**Abstract:** This paper investigates the effect of temperature on the microstructure, failure mechanism and compressive mechanical properties of newly developed ZA27 syntactic foams. Two different types of filler particles are considered, i.e. expanded perlite (P) and expanded glass (G). Metallic syntactic foam (MSF) has been produced via a counter-gravity infiltration process of packed particle beds, followed by controlled thermal exposure. Quasi-static compressive tests were carried out on cylindrical samples at five different in-situ testing temperatures between 25°C and 350°C. At all considered temperatures, P-MSF exhibits superior mechanical properties compared to G-MSF. The mechanical properties of both foam types decrease significantly with increasing testing temperature. For comparison, solid ZA27 samples were compressed at the same testing temperatures. Due to microstructural changes, a significant strength degradation of solid ZA27 was observed starting at 100°C. Comparison of results indicates that the temperature-dependent mechanical properties of P-MSF and G-MSF are strongly controlled by the matrix material. However, the addition of particles decreased the relative reduction of plateau stress and volumetric energy absorption of ZA27 MSF at elevated temperatures.

**Keywords:** quasi-static compression, metallic syntactic foams, expanded perlite/glass particles, temperature dependence, mechanical properties.

## 1. Introduction

Closed-cell porous materials, such as traditional metallic foams (TMFs) [1-4] and metallic syntactic foams (MSFs) [5-8], have gained significant attention in recent years in the context of replacing fully dense solid materials for structural and functional engineering applications [9-11]. Due to their cellular structure (low relative density) and unique ability to tailor mechanical/thermal/physical properties (higher stiffness-to-weight ratios, excellent energy absorption capacity, high vibration absorption, high specific strength etc.), the TMFs and MSFs have found favorable applications in the automotive, aerospace and railway industries [12-14]. A complex three-dimensional interconnected network of solid struts and membranes/plates (cell walls) makes up the foam meso-structure. It shows exclusive capacity to undergo very large deformation (up to 60-70% strain) at an almost constant stress in compression. As a result, these cellular structures are able to dissipate large amount of kinetic energy at low and nearly constant reaction loads [15, 16].

The effect of microstructure [17-19], heat treatment [20], particle shape [21], and particle size [22, 23] on mechanical/thermal/structural properties and deformation mechanisms of MSFs were investigated by different teams of researchers under static and dynamic loading conditions [24-28]. Kadar et al. [29] presents the analysis of the compressive deformation mechanisms of hollow ceramic spheres syntactic foams using the acoustic emission technique. Their analysis revealed three dominant deformation mechanisms: plastic deformation of the cell walls, sphere fracture and cell wall collapse. Taherishargh et al. [20] showed that heat treatment enabled a significant improvement of the mechanical properties of aluminum-based MSF. Also, due to their regular positioning and less structural defects, foams containing rounded perlite particles showed higher mechanical strength at a constant density [21]. In addition, the compressive deformation can be controlled by decreasing the particle size resulting in smoother and steeper stress-strain curves [22]. Orbulov [23] investigated the aspect ratio effect of the aluminum matrix syntactic foams specimens on their mechanical properties. He found a higher structural stiffness with increasing aspect ratio. Simultaneously, the fracture strain and the absorbed energy decreased significantly. Al-Sahlani and co-workers [30, 31] have investigated the effect of particle size (1-1.4, 2-2.8 and 4-5.6 mm) and particle shrinkage on the structural and compressive mechanical properties of recently developed expanded glass-metal syntactic foams (G-MSF). They found that the elastic stiffness and yield stress increase with particle size, while foams with smaller particles exhibit a near constant plateau stress and therefore a high-energy absorption efficiency. The authors observed that particle shrinkage is widely prevented by limiting the exposure time at high furnace temperatures ( $>600^{\circ}\text{C}$ ).

However, most of these papers have been thus far generally focused on room temperature testing conditions. To the author's knowledge, only a single study was performed on the temperature-dependent properties of closed cell ZA27 foam and no study on syntactic ZA27 foam has been published to date [32]. Thus, aspects such as elevated operating temperatures and related collapse mechanisms of MSFs are yet unfamiliar. In real world applications, foam composite work under different temperature conditions and the effect of high temperatures on their mechanical properties cannot be ignored. It has been shown previously that porous materials are very sensitive to temperature changes [33]. Therefore, understanding the mechanical behavior of ZA27 syntactic foams at elevated temperatures is critical for exploring their suitability for constructing lightweight composite structures.

The aim of the present work is to produce high strength MSFs with a novel matrix alloy and two different particle types (expanded perlite and expanded glass particles). Quasi-static testing is used to investigate the compressive foam properties at different in-situ testing temperatures. Furthermore, the foam microstructure together with failure mechanisms are assessed according to operating temperature.

## **2. Experimental details**

### **2.1. Raw material and foam sample preparation**

The commercially available Zinc-aluminum alloy ZA27 was selected as the matrix material of the syntactic foams. The chemical composition of the alloy was assumed to comply with ASTM B86 (see Table 1) [34]. This alloy has the lowest density compared to other zinc-aluminum alloys making it attractive for weight critical applications [35]. In addition, the alloy is heat-treatable allowing the targeted adjustment of the properties of the matrix material in metal syntactic foams. Aluminum is the major alloying element for this purpose [36]. In addition, aluminum improves the corrosion resistance of this material [37]. Copper is the second major alloying element in ZA27 alloy. Addition of copper produces the intermetallic compound  $\text{CuZn}_4$  ( $\epsilon$ -phase) in the inter-dendritic regions of the as-cast microstructure. The influence of  $\epsilon$ -phase on ZA27 properties is mostly evident after specific heat treatment procedures [37, 38]. These thermal treatments include solution treatment followed by water quenching to produce a super-saturated  $\beta$  phase. During subsequent aging, the  $\epsilon$ -phase is decomposed in a controlled manner and used to adjust the properties of the alloy. In the current study, such thermal treatment (i.e. rapid cooling) was not used and thus the impact of Cu on the microstructure and its properties is considered secondary and has been disregarded [38].

The influence of the trace elements Pb, Cd and Sn was considered negligible due to their very small amounts.

Two different types of particles with the same size range between 2-2.8mm were selected as the filler. The first particle type is expanded perlite (P). It is produced by heating volcanic perlite above its softening temperature so that the contained water is able to evaporate and expand the particles to 15-20 times of their initial volume. As a result, very low particle densities of 0.15-0.18 g/cm<sup>3</sup> are obtained [26]. The second particle type is expanded glass (G) which was produced and supplied by Poraver®. G particles have a higher particle density of 0.33 g/cm<sup>3</sup> [31] and a significantly higher strength. The crushing strength of G particle beds at 30% strain is about 1-2 MPa [30] compared to less than 0.5 MPa [39] in the case of P particle beds.

Table 1. Chemical composition of ZA27 alloy [35]

Element	Al	Cu	Mg	Fe	Pb	Cd	Sn	Zn
wt.%	25.0-28.0	2.0-2.5	0.01-0.02	0.075	0.006	0.006	0.003	Balance

P-MSF and G-MSF samples (see Fig. 1) were produced via a counter-gravity infiltration process that is described in detail in a previously published paper [17]. To ensure optimum infiltration and to minimize the evaporation of Zn, the casting temperature was empirically adjusted to 535°C. Following solidification, the samples were labelled and machined on both ends to achieve a universal height/diameter ratio of approximately 1.6± 0.04.

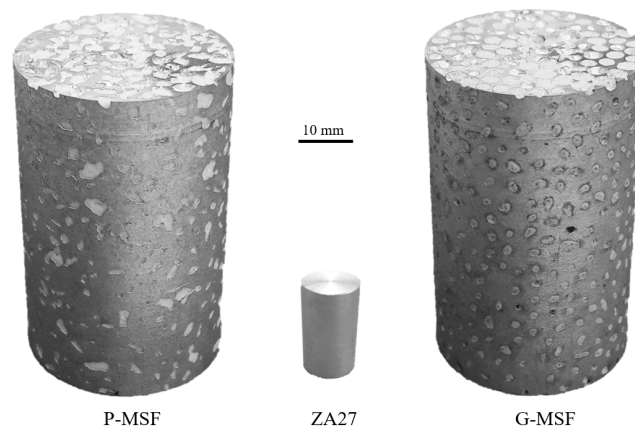


**Fig. 1.** Samples: P-MSF (left), solid ZA27 (center), and G-MSF (right)

The manufactured 30 samples (15 P-MSF and 15 G-MSF) were divided into five groups whereas each group was exposed to a different temperature range. The targeted temperatures coincide with the testing temperatures, i.e. 25 (or ambient), 100, 200, 300 and 350°C. All

samples were held inside a furnace at the respective targeted temperature for 48 hours before cooling to room temperature at atmospheric conditions. This extensive holding time was chosen in order to eliminate transient effects and permit the completion of any phase transition. Prior to mechanical testing (see next Section), samples were reheated and held at their respective testing temperature for 90 minutes. This heat treatment intends to simulate exposure to a high-temperature environment during application.

The macroscopic volume  $V_{SF}$  of each sample was determined by measuring its height  $h$  and diameter  $d$  at several locations and using average values to calculate  $V_{SF} = h \cdot \pi d^2 / 4$ . The sample mass  $m_{SF}$  was measured on a precision scale (accuracy  $\pm 0.1$  mg) and the sample density obtained as  $\rho = m_{SF} / V_{SF}$ . The geometrical dimensions and physical properties of all samples are summarized in Table 3 of the Appendix. The volume fractions of the matrix ( $\phi_{ZA27}$ ), particles ( $\phi_P$ ) and voids ( $\phi_V$ ) of the syntactic foams were calculated using the following equations [31]:

$$\phi_{ZA27} = \frac{m_{SF} - m_P}{\rho_{ZA27} V_{SF}} \quad (1)$$

$$m_P = \rho_B \cdot V_{SF} \quad (2)$$

$$\phi_P = \frac{\rho_B}{\rho_P} \quad (3)$$

$$\phi_V = 1 - \phi_{ZA27} - \phi_P \quad (4)$$

where  $\rho_B$  and  $\rho_P$  are the bulk and envelope densities of the particles, respectively. According to [35] the density of ZA27 matrix was considered to be  $5.00 \text{ g/cm}^3$ .

## 2.2. Quasi-static compression tests

Uniaxial quasi-static compression tests were carried out on cylindrical solid ZA27 and metallic syntactic foam samples (diameter  $\approx 27$  mm and height  $\approx 43$  mm, see Fig. 1) using a universal LBG testing machine equipped with a thermal chamber and a 100 kN load-cell. The dimensions of the samples were chosen in such a way that each spatial direction contains at least ten cells (particles) to minimize size effects [40]. The experimental tests were performed with a constant crosshead speed of 10 mm/min inside a furnace at five different testing temperatures, i.e.  $25^\circ\text{C}$ ,  $100^\circ\text{C}$ ,  $200^\circ\text{C}$ ,  $300^\circ\text{C}$  and  $350^\circ\text{C}$ . In order to test the reproducibility and reliability of the results, three samples were investigated at each test temperature. The experimental procedure was designed in such a way that the all samples reached a homogenous

temperature distribution prior to compression. For this purpose, all samples were preheated in the thermal chamber for 90 minutes at the respective testing temperature. In order to prevent any reduction in temperature after preheating, the foam samples were compressed inside the thermal chamber. The deviation from each test temperature was within  $\pm 3^\circ\text{C}$ .

The identical experimental procedure was used for the mechanical characterization of the matrix material. To this end, cylindrical solid ZA27 samples with a diameter of 10 mm and a height of 16 mm were machined out of the solidified excess melt from the MSF casting. This approach ensured that the solid samples followed the same thermal history as the MSF samples and exhibit a micro-structure similar to the foam struts. The size of the sample was reduced due to the increased sample strength and the testing machine limitation to 100 kN; however, the aspect ratio of the foam samples was maintained.

The testing temperatures were chosen in such a way that the investigated ZA27 alloy passes through several phases of the Zn-Al binary equilibrium phase diagram. In the ZA27 alloy, the  $\alpha$  phase (Al) + liquid (L) forms above  $\sim 418^\circ\text{C}$ . Below this temperature, the  $\beta$  phase (ZnAl) is stable until  $315^\circ\text{C}$ . Below  $315^\circ\text{C}$ , a fraction of the  $\beta$  phase separates into  $\alpha$  and  $\beta$  until  $275^\circ\text{C}$ , when the eutectoid transformation  $\beta$  (ZnAl)  $\rightarrow$   $\alpha$  (Al) +  $\eta$  (Zn) occurs. Below  $275^\circ\text{C}$ ,  $\alpha$  (rich in Al) +  $\eta$  (rich in Zn) is formed [41]. The planned experimental tests will thus consider the ZA27 phases presented in Table 2.

Table 2. Testing temperatures and ZA27 phases

Testing temperature [ $^\circ\text{C}$ ]	Phase area	
25	$\alpha+\eta$	$\alpha$ : Al rich phase (fcc) $\beta$ : Zn rich phase (fcc)
100	$\alpha+\eta$	
200	$\alpha+\eta$	$\eta$ : Zn rich phase (hcp)
300	$\alpha+\beta$	
350	$\beta$	

The compressive mechanical properties were determined from the compressive stress-strain data following ISO 13314 [42]. The plateau stress  $\sigma_{Pl}$  is selected as the arithmetical mean of the stresses between 20% and 40% compressive strain. The volumetric energy absorption capacity  $W$  is obtained by integration of the stress strain curve (see Eq. 5) up to 50% strain and can be interpreted as the area underneath the curves [1, 28, 43]. The volumetric energy absorption can alternatively be calculated using variable integration limits.

$$W = \int_0^{50\%} \sigma d\varepsilon \quad (5)$$

Moreover, the energy absorption divided by the product of the maximum compressive stress  $\sigma_{\max}$  up to 50% macroscopic strain and the strain value itself is named energy absorption efficiency  $\eta$  [42]:

$$\eta = \frac{\int_0^{50\%} \sigma de}{\sigma_{\max} \cdot 50\%} \quad (6)$$

### 3. Results and Discussion

#### 3.1. Physical properties of MSF samples

The density of the produced metal syntactic foams varied from 1.983 to 2.145 g/cm<sup>3</sup> for P-MSF and 1.746 to 1.882 g/cm<sup>3</sup> for G-MSF. As expected, the addition of expanded perlite and expanded glass to the ZA27 matrix significantly decreased the material density. The foam densities of this study are well below zinc based syntactic foams (3.3 to 5.1 g/cm<sup>3</sup>) produced via stir casting [44]. The distinctly higher density of the zinc foams reported in [44] could be related to the fracture and filling of micro-balloons with molten metal during production. In contrast, damaged P and G particles of the current study do not fill completely with metal during infiltration casting. The volume fraction of ZA27 matrix and voids in each syntactic foam sample were calculated using equations (1) and (3). According to Table 3 in the Appendix, it is apparent that the matrix volume fraction of P-MSF (average value 39.62%) distinctly exceeds G-MSF (average value 32.50%). Conversely, the void fraction in P-MSF is significantly lower than in G-MSF foam. This is most likely related to differences in the inter-particle channel thickness and particle surface tension, which affects the infiltration of molten ZA27 [45].

#### 3.2. Compressive properties of solid ZA27 samples

Compression tests of solid ZA27 samples were conducted at the testing temperatures 25, 100, 200, 300 and 350°C. The obtained quasi-static compressive stress-strain curves of these solid samples are plotted in Fig. 2a (one sample was tested for each temperature). All curves show a linear-elastic region with a smooth transition into a stress plateau.

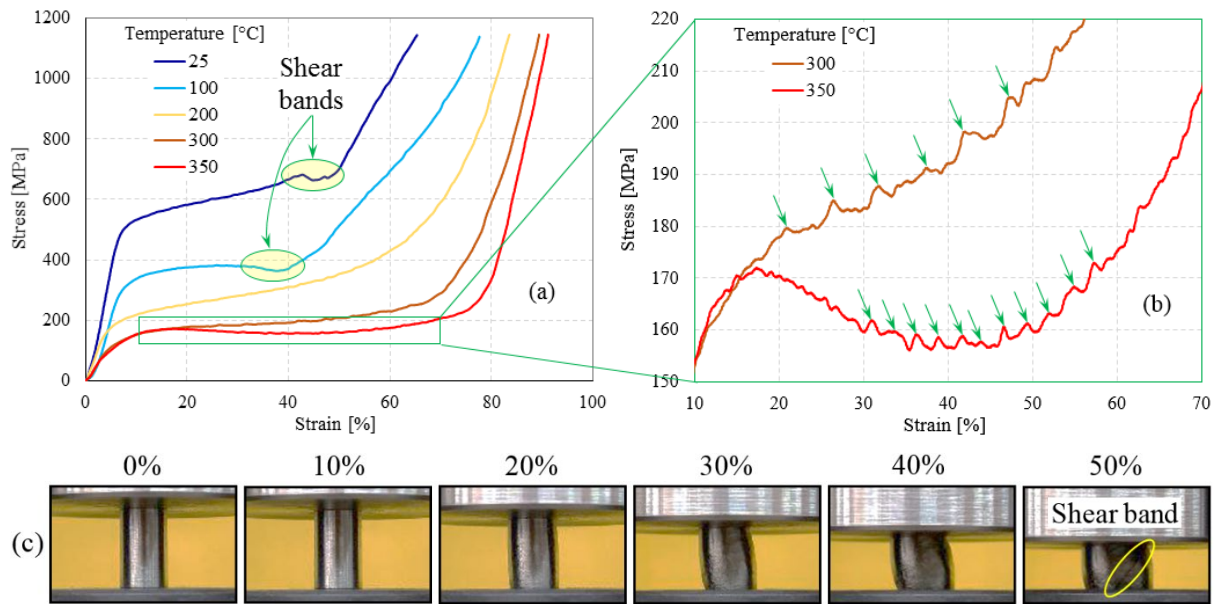


**Fig. 2.** Solid ZA27: (a) compressive stress-strain data, (b) magnified stress-strain curves, (c) deformation sequence at 25°C

Temperature increase clearly decreased the compressive stresses of all samples. The biggest change in stress-strain behavior was observed between 25→100°C. This difference between temperatures (100→200°C, 200→300°C and 300→350°C) decreases with increasing test temperature. Notably, only a minor stress reduction occurs between 300→350°C.

Figure 2c shows photographs captured during the room-temperature compression of solid ZA27 sample. No images are available for higher temperatures due to the compression inside a furnace chamber. At room temperature, the samples initially barreled due to friction with the compression platens. At 40-50% macroscopic strain, a macroscopic shear bands emerges in the form of a crack orientated at an angle of approximately 45° relative to the loading direction. This shear band is also visible in the stress strain data (see Figure 2a) as a distinct stress oscillation.

At 100°C the stress-strain curve (Fig. 2a) still shows oscillations but their amplitude is significantly lower than at 25°C. The compressed sample reveals a shear band at 45° relative to loading direction (see Fig.3b, 100°C). The microstructure of the ZA27 at 25°C (Fig. 3a) shows sharp and needle-like primary dendrites, which decrease its ductility [46]. Heating the samples to 100°C coarsens the primary dendrites and some parts of the microstructure have transformed to a more spheroidized morphology. This microstructural alteration reduces the brittleness of the alloy [47]. As a result, the flow stress and hardness of the alloy are reduced.

At 200°C the flow stress of solid ZA27 alloy is significantly lower than at 25°C and 100°C. This fact is most likely related to the dynamic recrystallization of the ZA27 alloy at 200°C and higher temperatures. Dynamic recrystallization is one of the typical softening mechanisms of metallic alloys and occurs during deformation at elevated temperatures [48]. Sahu et al reported that the dynamic recrystallization of ZA27 starts at approximately 200°C [49]. The optical images of the compressed ZA27 alloy at 200°C (Fig. 3) show a plastically highly deformed (i.e. flatter) sample with some peripheral cracks due to shear deformation in conjunction with strong barreling during compression.

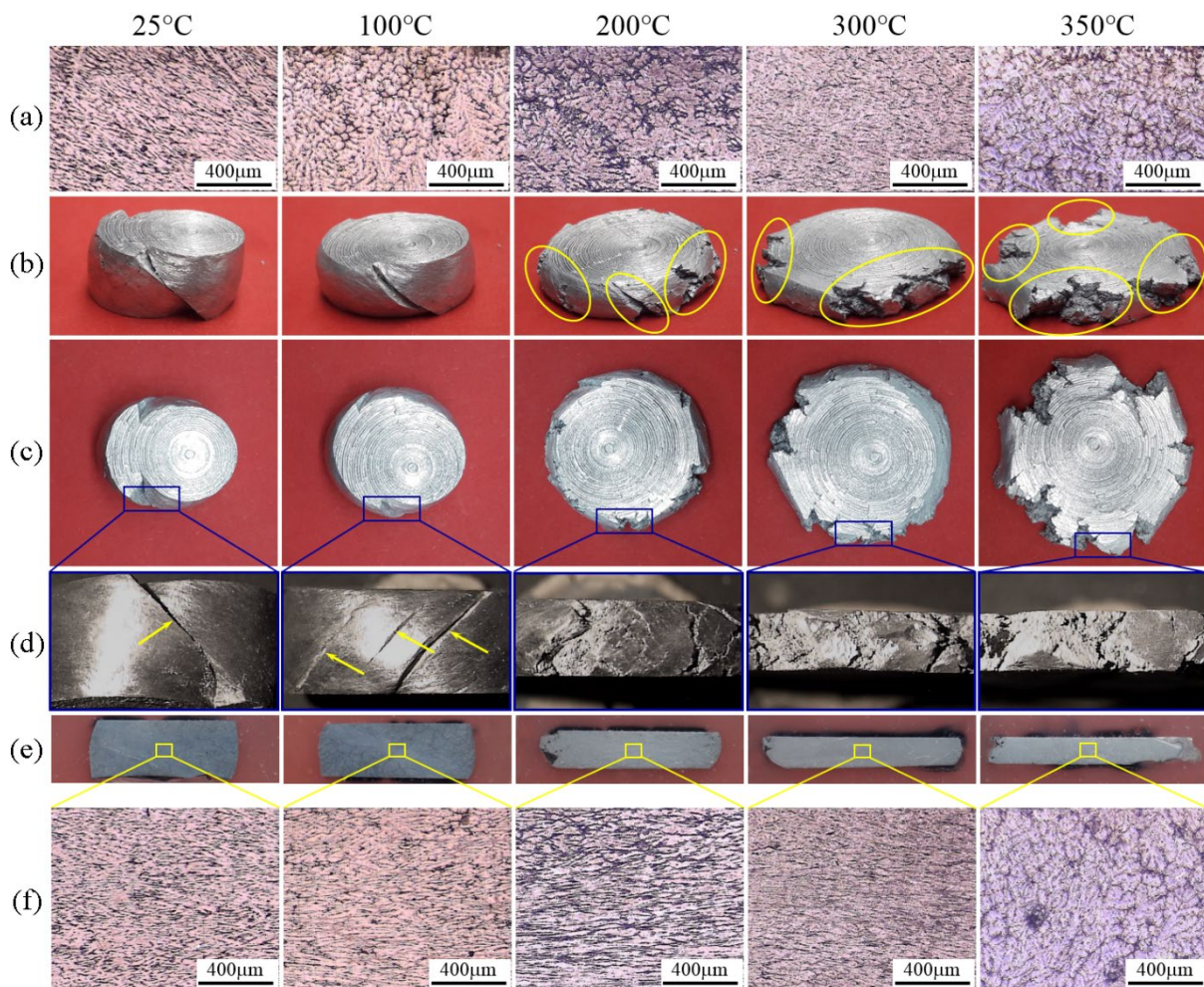


**Fig. 3.** Microstructure of ZA27 alloy before compression tests (a); Isometric (b), top (c) and lateral (d) view of deformed solid ZA27 samples; sample cross-section (e) and microstructure of deformed samples (f) at different testing temperatures

A temperature increase to 300°C and 350°C further decreases the strength of the alloy. At higher temperatures, the mobility of grain boundaries for nucleation and the growth rate of

dynamically recrystallized grains increases and thus decreases the flow stress of the alloy [50]. In addition, at 300°C and 350°C low amplitude stress oscillations reoccur (see Fig. 2). This is attributed to the increasing brittleness of ZA27 alloy at these temperatures due to formation of the zinc-rich  $\beta$  phase in the microstructure of the alloy. The increasing volume fraction of the  $\beta$  phase gradually changes the deformation mechanism of ZA27 from ductile at 200°C to quasi-brittle at 350°C. The optical images of the compressed samples at 300°C and 350°C (see Fig. 3) show evidence of sample fragmentation and the occurrence of multiple macroscopic shear failure regions. This failure mechanism indicates the brittleness of the ZA27 alloy near its melting temperature. Moreover, coarsening of the microstructure at this temperature is obvious in Fig. 3a, 350°C.

In summary, the following phenomena are observed in solid ZA27 due to increasing temperature:

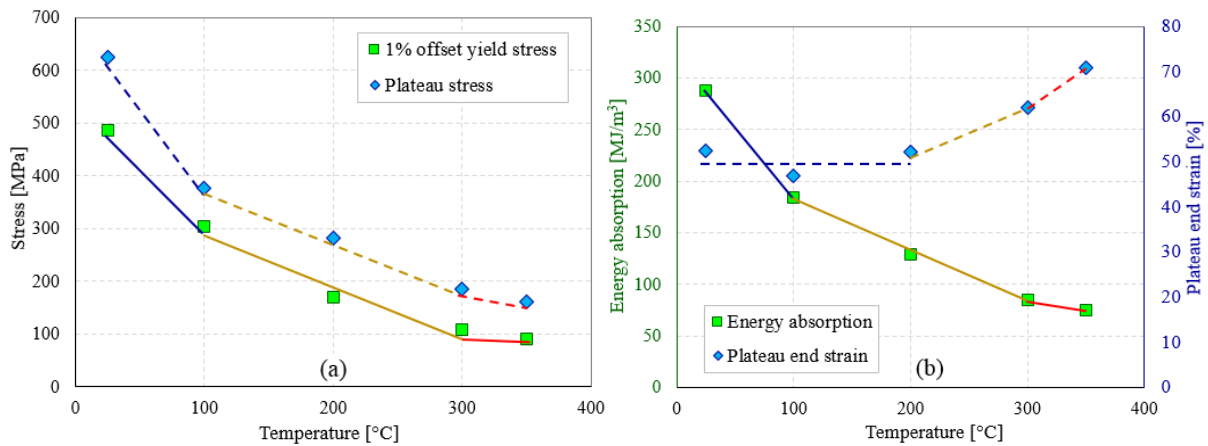
- Starting at 100°C: softening due to microstructure coarsening and spheroidization
- Starting at 200°C: softening due to dynamic recrystallization
- Starting at 300°C: increasing brittleness because of phase transitions

Figure 3e shows cross-sections of deformed ZA27 samples. Compared to the initial microstructure (see Fig. 3a), the grain boundaries of deformed solid samples tend to elongate and flatten (Fig. 3f). This flattening is more pronounced up to 200°C and seems reduced at higher temperatures, most likely due to dynamic recrystallization of the microstructure.

Figure 4 shows the material properties of solid ZA27 plotted versus the testing temperature. The plateau stress and 1% offset yield stress (see Fig. 4a) decrease rapidly from 25°C→100°C (blue lines). At higher temperatures, a linear decrease is observed up to 300°C (brown lines). Between 300→350°C only a minor stress reduction occurs (red lines). A very similar trend is observed for the volumetric energy absorption in Fig. 4b. The rapid decline between 25°C→100°C can be explained by the spheroidization of the microstructure described above. The subsequent linear decline is caused by the continuing transition from brittle to ductile behavior. However, a further increase of the testing temperature from 300°C→350°C results merely in a minor additional softening of the alloy. A likely explanation is the microstructural formation of the brittle  $\beta$  phase that partially counteracts the strength decrease due to spheroidization and dynamic recrystallization.

The plateau end strain (see Fig. 4b) is relatively low up to 200°C (around 50% strain). At higher temperatures, the plateau end strain increases progressively, reaching a value of 70.82% at 350°C. A likely explanation is dynamic recrystallization that suppresses work

hardening resulting in the more constant plateau stress compared to lower temperatures visible in Fig. 2.



**Fig. 4.** Mechanical characteristics of solid ZA27 samples at different temperatures:  
 (a) stresses, (b) energy absorption and plateau end strain

### 3.3. Compressive properties of MSF samples

In this section, the results for the compressive testing of MSF samples are presented. To evaluate the effect of the particle type, two different foams with either expanded perlite (P) or expanded glass (G) particles were tested. Fig. 5a shows typical compressive stress-strain curves of P-MSF (full lines) and G-MSF (dashed lines). For clarity, only one of the three tested samples per foam type and temperature is drawn. Figure 5b presents photographic images captured during the 25°C compression at 10% macroscopic strain intervals.

During quasi-static compression, the typical stress-strain curves of cellular materials are obtained. The curves may be divided into three distinct deformation regions [51-53]: a narrow linear elastic region occurs at small strains (typically 5% or less) where the stress rises sharply before either reaching a stress peak or deviating from linearity. This first region is followed by an extended collapse plateau region with only a small stress increase over a large deformation (up to approximately 60% strain). Within the plateau region, the deformation resistance is approximately constant, and for this reason, the stress plateau is attractive for crash-protection and energy-absorption systems. Finally, the stress-strain curve ends with a region of densification, accompanied by an abrupt stress increase due to cell wall interactions [16, 54]. These deformation regions are observed regardless of particle type or testing temperature.

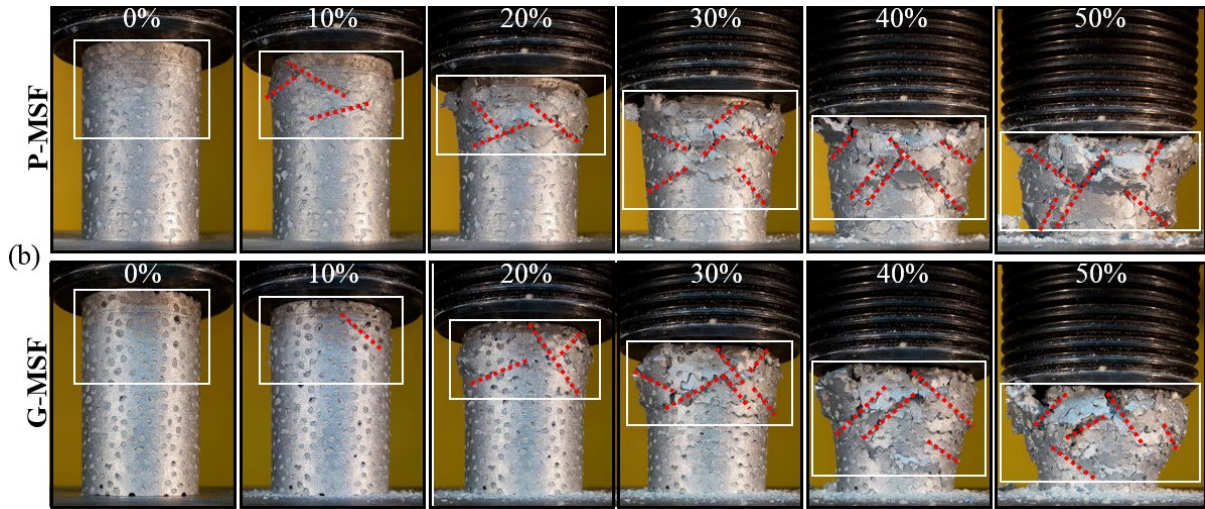
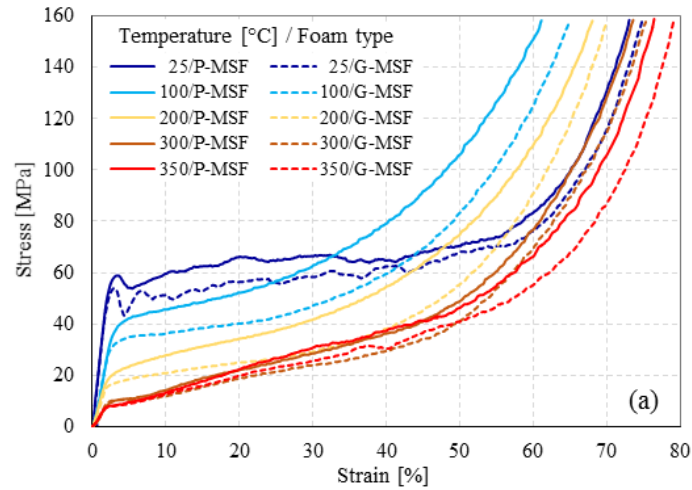


**Fig. 5.** Compression of P-MSFs and G-MSFs at different temperatures:  
 (a) stress-strain data, (b) deformation sequence at 25°C.

At all tested temperatures, the stress-strain curves of P-MSF are above G-MSF. This systematic difference can be explained by the higher matrix volume fraction and lower void fraction of the ZA27 matrix in P-MSF (see Table 1).

### 3.3.1. Deformation mechanism of MSF samples at 25°C (room temperature):

At 25°C, the compressive stress-strain graphs of P-MSF and G-MSF exhibit a peak stress  $\sigma_{Peak}$  at the end of the linear-elastic region. This peak stress is followed by a distinct stress drop that is attributed to brittle fracture and the formation of shear crack at low macroscopic strains (see Fig. 5b at 10% strain). Moreover, the stress-strain curves at 25°C (Fig. 5a) exhibit a serrated stress plateau. Both phenomena can be explained by the brittle deformation behavior of the ZA27 matrix at 25°C due to its sharp dendritic microstructure (see Section 3.2). The compression of P-MSF and G-MSF is accompanied by the formation of

macroscopic shear cracks because of cell-wall failure through bending, buckling and, importantly, brittle fracture. These shear bands are clearly visible in Fig. 5b and result in an almost constant plateau stress for both P-MSF and G-MSF samples. Compared to solid ZA27, the first shear bands occur at relatively low macroscopic strains. This is caused by the concentration of plastic deformation in small sub-volumes of the ZA27 matrix resulting in high local deformation. The surface cracks originate in all MSFs samples near the upper sample surface. This surface is opposite the infiltration surface during casting, i.e. the metallic melt infiltrated this volume last. The initiated cracks progressively spread and form macroscopic shear bands at different angles, which finally form global collapse regions [31]. At high strains, the 25°C samples exhibit multiple shear bands that eventually merge and result in partial fragmentation (see Fig. 5b, 50% strain).

### 3.3.2. Deformation mechanism of MSF samples at elevated temperatures:

At higher temperatures (100-350°C), the engineering stress-strain curves show an indistinct yield point without any visible stress peak (see Fig. 5a). This can be explained by a significant increase in ductility of the matrix (see Section 3.2) that suppresses brittle fracture of cell walls and matrix struts and thus the early formation of shear cracks. Instead, the matrix undergoes increased plastic deformation, albeit at a decreased flow stress.

At moderate temperatures  $T \geq 100^\circ\text{C}$ , the serrated morphology of the stress-strain graphs gradually transitions into a smoother curve (see Fig. 5a) indicating a more ductile deformation. A similar brittle to ductile transition with increasing temperature was observed for various types of aluminum foams, i.e. as-cast A356 aluminum alloy closed-cell foams [32, 42, 55], closed cell aluminum foams (Al99.5, AlMg1Si0.6 and AlSi12 matrix alloys, TiH<sub>2</sub> foaming agent) prepared by powder metallurgy [56, 57], and expanded perlite/A356 aluminum syntactic foams produced via a counter-gravity infiltration process [25]. Deformed P-MSF and G-MSF samples (see Fig. 6 at 100°C) show increased plastic deformation in comparison to the room-temperature samples with only minor signs of cracks and matrix detachment.

At 200°C, plateau stress oscillations are further decreased regardless of the particle type (see Fig. 5a). Similar to solid ZA27, the maximum stress decrease occurs between 100°C and 200°C, which is likely related to initiation of dynamic ZA27 recrystallization at 200°C. The optical inspection of the deformed samples at 200°C (see Fig. 6) indicates a further increased ductility compared to 100°C (Fig. 6, 200°C).

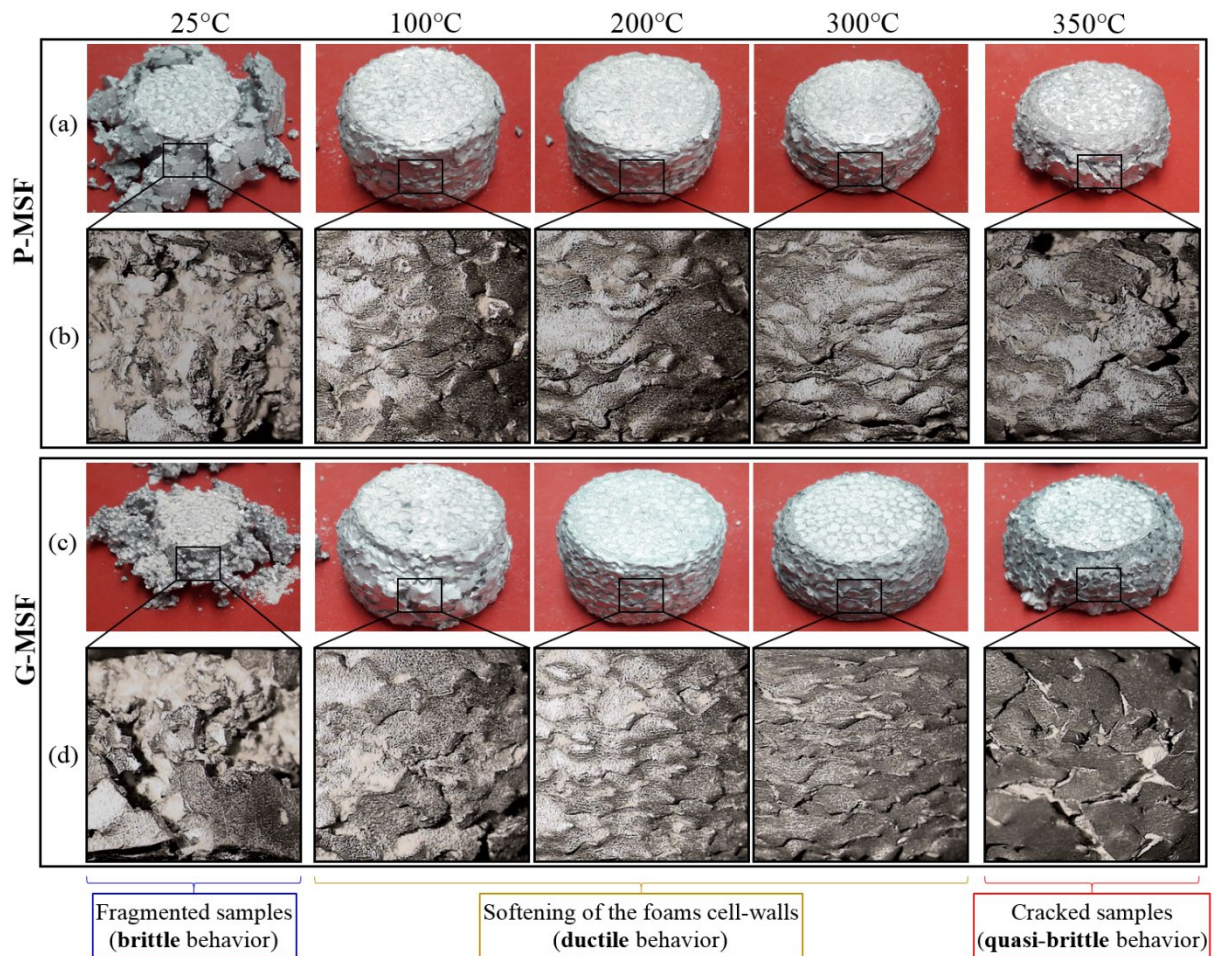


**Fig. 6.** Deformed P-MSFs (a) and G-MSFs (c) samples after different testing temperatures, and optical images (b, d) of the outer sample surfaces (magnification 8x)

Increase of the testing temperature to 300°C results in an additional stress reduction. However, no significant deviation is found between 300°C→350°C. In addition, minor plateau stress oscillations reemerge at these elevated testing temperatures (especially within the stress plateau between 25% and 50% strain). These oscillations exhibit a non-periodic character and a small amplitude compared to those observed at room temperature. Analyzing Fig. 6, it is evident that brittle fracture reemerges at 300-350°C, i.e. signs of cell wall cracks are detected regardless of particle type. As described for solid ZA27, the transition from  $\alpha+\eta$  to  $\alpha+\beta$  and  $\beta$  regions gradually decreases the fraction of the ductile  $\alpha$ -phase in the ZA27 microstructure. At 350°C the ductile  $\alpha$ -phase is completely replaced by the brittle  $\beta$ -phase, which decreases the ductility of the matrix and thus of the syntactic foam.

### 3.3.3. Microstructural analysis of deformed MSF samples

Figure 7 presents optical and SEM images of the cross-section of deformed P-MSF and G-MSF samples. The microstructure of P-MSF after compression at 25°C shows distinct microcracks (region C1). This is in good agreement with the macroscopically observed brittle deformation of solid ZA27 and MSF. At 200°C, plastic deformation is much more pronounced compared to 100°C and 25°C.

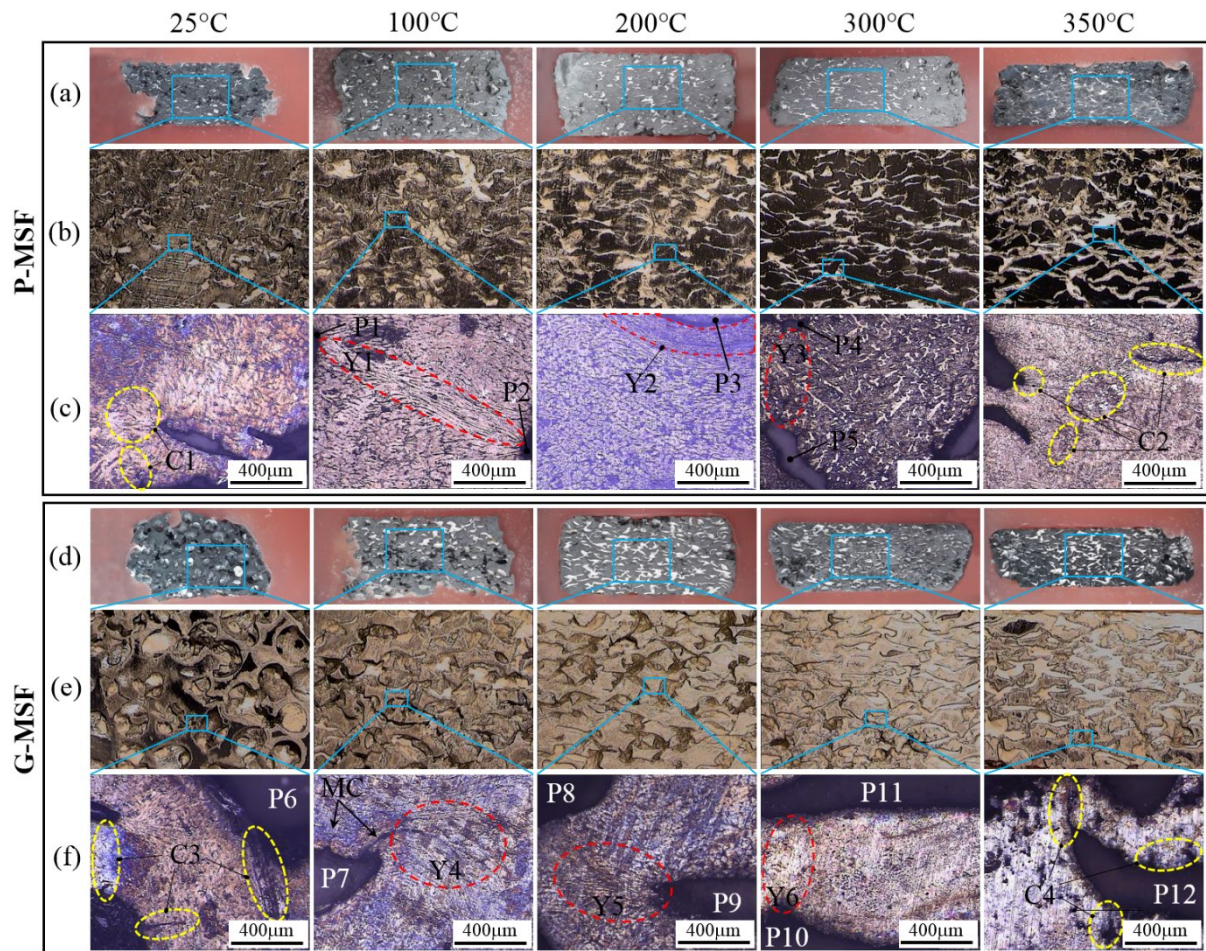


**Fig. 7.** Cross-sections of deformed MSF: (a, d) photographs, (b, e) stereographic view (8x magnification), (c, f) SEM images

At a microstructural level, texture formation occurs (Y2) indicating a high degree of plastic deformation. At 300°C, the yield area (Y3) is less pronounced, which is likely caused by the ZA27 embrittlement due to the formation of the  $\beta$ -phase. At 350°C, quasi-brittle deformation of solid ZA27 occurs (Figs. 2 and 3). The brittle ZA27 deformation coincides with the reemergence of micro-crack regions in the P-MSF micro-structure (C2). Near identical crack (C3, C4) and yield (Y4-6) regions were observed in G-MSF indicating that the particle

type does not influence the deformed microstructure of the ZA27 foam matrix. Regardless of foam type, all the main collapse mechanisms (plastic deformation, micro-cracks) have occurred around the foam pores (P1-P12).

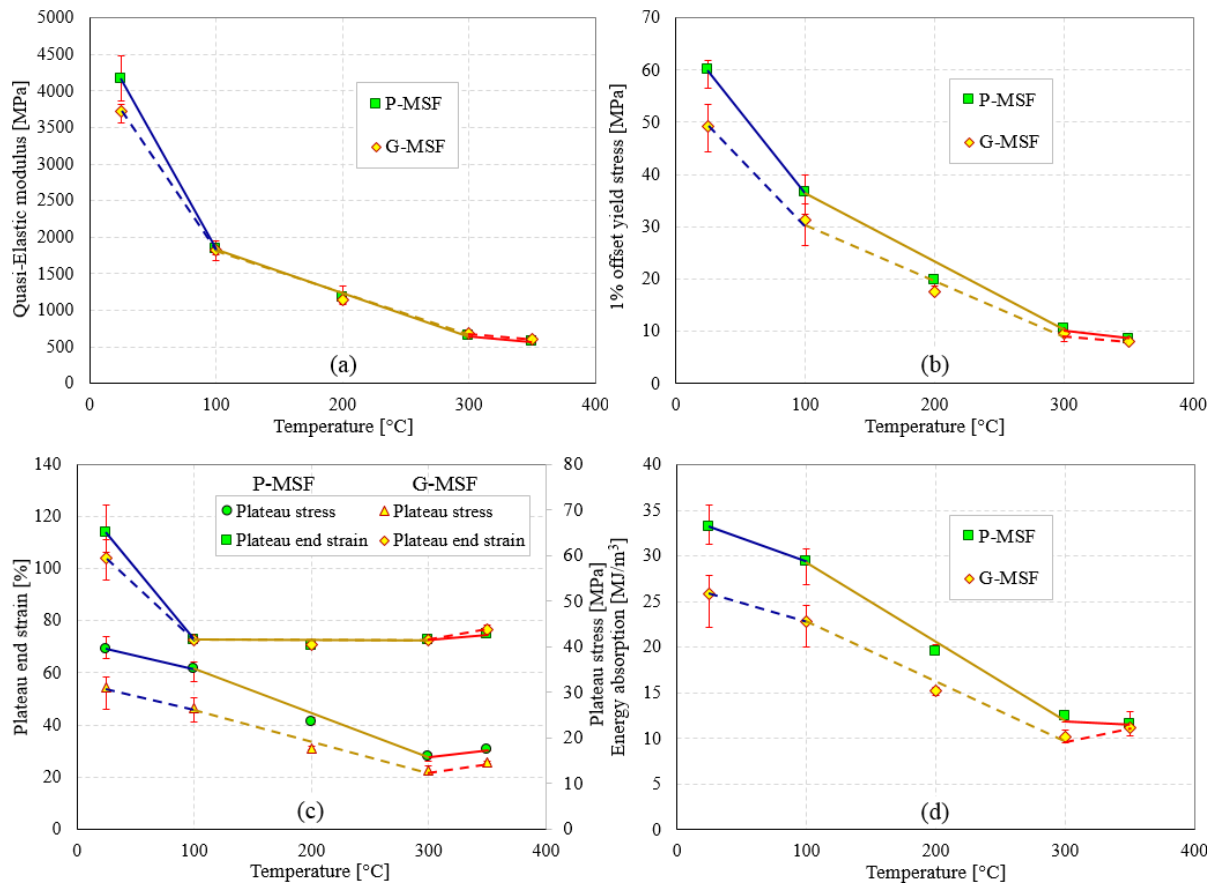
#### 3.3.4. Mechanical properties of MSF samples

Figure 8 presents the mechanical properties of MSF at various temperatures. P-MSF and G-MSF show similar patterns for all considered material properties. With the exception of the quasi-elastic modulus (where both foams exhibit similar absolute values), the mechanical properties of P-MSF are superior to G-MSF. This seems counter-intuitive, as the mechanical strength of expanded glass is higher compared to expanded perlite. However, G-MSF exhibits a distinctly lower matrix volume fraction compared to P-MSF (see Table 1). The strength of ZA27 significantly exceeds the strength of the glass particles and thus the decreased matrix volume fraction outweighs the higher particle strength. In addition, G-MSF contains a higher void volume fraction. Voids are likely to cause stress concentrations within the ZA27 matrix and initiate micro-cracks (MC) that further decrease the strength of G-MSF (for example see Fig. 7f at 100°C). At 25°C, a scattering of all mechanical properties (see error bars in Fig. 8) is observed due to brittle foam behavior. At higher temperatures (100→350°C) the scattering of the mechanical properties decreases significantly which can be explained by increasing ZA27 ductility (see Section 3.2). As expected, mechanical properties generally deteriorate with increasing temperature. However, above 300°C properties stabilize or even slightly increase. The quasi-elastic modulus and 1% offset yield stress reduce sharply from 25°C to 100°C. As discussed earlier, the 25→100°C transition coincides with a significant decrease of foam strength due to microstructure spheroidization (see Fig. 3a at 25 and 100°C). The material properties decrease further with increasing temperature, albeit at a lower rate.

The plateau stress and volumetric energy absorption only show a minor decrease from 25→100°C. Instead, and similar to solid ZA27, the biggest change is observed between 100→200°C. This temperature region coincides with a significant increase of ZA27 ductility that controls the flow stress at high strains. The emergence of the brittle  $\beta$ -phase causes a minor property increase between 300→350°C.

The relatively high densification strains >60% of both P-MSFs and G-MSFs at 25°C (see Fig. 8c) are caused by the brittle shear failure mechanism at this temperature (see Fig. 5b). The formation of macroscopic shear bands permits the sample to deform via sliding across one or multiple shear planes at a near constant resistance resulting in a constant and prolonged

stress plateau. Increasing the temperature to 100°C distinctly decreases the plateau end strain. Further temperature increase beyond 100°C does not significantly change the plateau end strain. This is likely due to a change of the deformation mechanism caused by increasing matrix ductility. Higher temperatures suppress the formation of catastrophic shear cracks that cause sample separation. Instead, the material becomes more ductile and the cells are plastically deformed instead of the sample fracturing and sliding across a macroscopic shear band. Due to the increased deformation of the cells, densification then occurs at a lower strain. The quasi-brittle transition at 300°C does not seem to affect this behavior. It can further be noted that despite differences in their matrix volume fraction, the densification strains of P-MSF and G-MSF are near identical.



**Fig. 8.** Mechanical properties of P-MSF and G-MSF: (a) quasi-elastic modulus, (b) 1.0% offset yield stress, (c) plateau end strain / plateau stress, (d) energy absorption

#### 4. Comparative Analysis

Figure 9 illustrates the reduction of stiffness, strength and energy absorption at different temperatures relative to room temperature. The highlighted areas represent the different sample

deformation mechanisms that occur during the quasi-static compression tests: I-brittle, II-ductile, and III-quasi-brittle behavior. Two transitions were observed: brittle to ductile (B→D) between 25°C and 100°C and ductile to quasi-brittle (D→QB) between 300°C and 350°C. In addition, the equilibrium phases of the ZA27 alloy are shown.

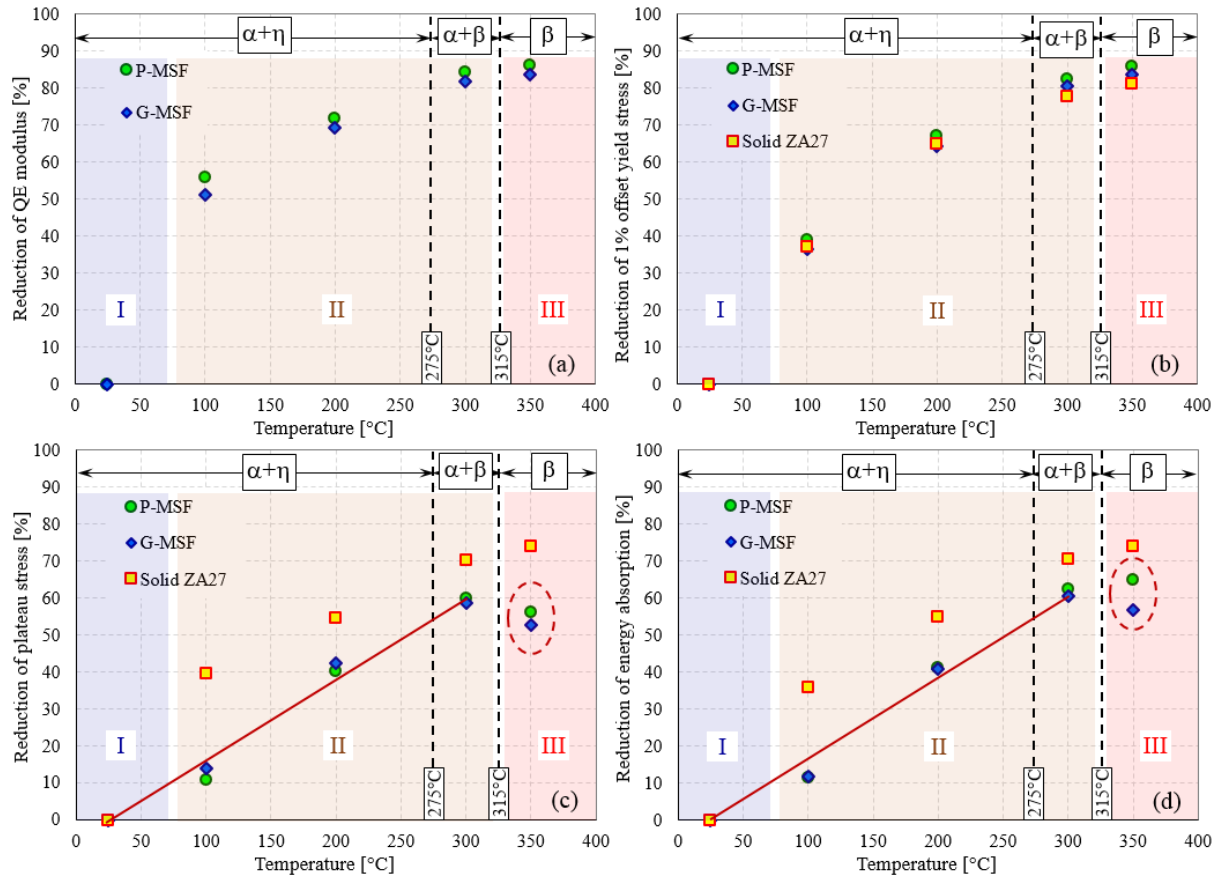


**Fig. 9.** Reduction percentage of quasi-elastic modulus (a), 1% offset yield stresses (b), plateau stress (c) and energy absorption (d) for MSFs and solid ZA27 samples at different temperatures normalized by 25°C values

### Quasi-elastic modulus

According to Fig. 9a, P-MSF and G-MSF show a similar relative reduction of their quasi-elastic moduli. The largest change occurs between 25→100°C. As described earlier, the ZA27 microstructure transitions to a spheroidized morphology in this temperature range which likely plays a role in this reduction. At higher temperatures, the sensitivity of the elastic modulus to temperature decreases albeit further reduction still occurs. The similar behavior of P-MSF and G-MSF suggests that the elastic foam behavior is widely independent of the particle type. However, the reduction of G-MSF is slightly below P-MSF, which could be related to the

higher stiffness of the expanded glass particles compared to expanded perlite. Both particles are unlikely to show significant changes of their mechanical properties within the considered temperature range, as the maximum test temperature 350°C is well below their softening temperature (>800°C). Hence, the particle contribution to the overall MSF stiffness is likely to increase with temperature. Due to their lower porosity, the elastic stiffness of expanded glass particles exceeds expanded perlite, resulting in the marginally lower stiffness reduction of G-MSF.

#### 1% offset yield stress

The MSFs and solid ZA27 show a near identical relative strength reduction. This is a strong indicator that the mechanical strength of the foams and its variation with temperature is governed by the matrix material. The highest strength reduction occurs between 25→200°C. This temperature region coincides with the microstructural transition of ZA27 from needle-like primary dendrites to a more spheroidized morphology (see Section 3.2). From 200→350°C the strength decreases only gradually. This is most likely due to the emergence of the brittle  $\beta$ -phase that exhibits a higher resistance to plastic deformation and thus partially counteracts the microstructural softening.

#### Plateau stress and volumetric energy absorption

Based to their definition, these material properties are quite similar and are thus discussed together. Both capture the deformation resistance of a material at higher strains. Considering the MSF, a linear strength decrease of both properties is found up to 300°C. This properties decrease is given by Eqs. (7) and (8).

$$\sigma_{pl,R} = 0.227 \cdot T [\text{°C}] - 7.7179, \quad \text{with } R^2 = 0.988 \quad (7)$$

$$W_R = 0.229 \cdot T [\text{°C}] - 7.4468, \quad \text{with } R^2 = 0.989 \quad (8)$$

The underlying mechanism is the ZA27 softening discussed in Section 3.2. In particular, dynamic recrystallization has a strong impact on the stress plateau due to the higher degree of plastic deformation. However, this effect does not strongly affect the offset yield stress (i.e. the onset of plastic deformation) which explains the differences in the respective trend lines in Fig. 9.

Interestingly, at 350°C an increase of the plateau stress and the volumetric energy absorption is found relative to 300°C. The temperature increase 300→350°C corresponds to the completion of the microstructural transition into the brittle  $\beta$ -phase. As evident in Fig. 5, this

increases the stresses at higher strains resulting in an increased plateau stress and volumetric energy absorption. Below 350°C, both P-MSF and G-MSF exhibit near identical trend lines suggesting once more that foam properties are predominantly controlled by the matrix material. However, at the  $T = 350^\circ\text{C}$ , G-MSF shows a decreased property reduction. A possible explanation is that the compression of the stronger expanded glass particles increases the deformation resistance of G-MSF at high strains. Due to the high thermal stability of the particles, this effect is most pronounced at the maximum test temperature.

Comparing solid ZA27 to the MSFs, solid ZA27 undergoes a significantly higher reduction of the plateau stress and volumetric energy absorption at all temperatures. The maximum deviation is found at 100°C. The volumetric energy absorption and plateau stress are highly sensitive to the deformation mechanism. Earlier analysis revealed that solid ZA27 and MSF develop macroscopic shear bands that provide sliding planes for sample deformation. This sliding mechanism permits compression at a near constant stress up to high strains (see Fig. 2). Microstructure spheroidization and dynamic recrystallization of ZA27 increases ductility and promotes the formation of multiple shear bands in solid ZA27 (see Fig. 3). This could explain the strong property reduction in solid ZA27. In MSF, embedded particles seem to interrupt the growth of macroscopic shear planes and instead promote the plastic deformation of cell walls. The increased plastic deformation then results in a higher energy absorption per unit volume.

## 5. Conclusions

1. The manufactured P-MSF is stronger than G-MSF at all tested temperatures. The explanation is the higher ZA27 matrix volume fraction of P-MSF.
2. ZA27 alloy and its syntactic foams undergo brittle shear failure at 25°C. This results in a near-constant average plateau stress with distinct oscillations.
3. Commencing at 100°C, spheroidization of the ZA27 microstructure is observed. This causes a distinct strength reduction and ductility increase of ZA27 and its MSFs.
4. Dynamic recrystallization of ZA27 is known to commence at 200°C. This phenomenon further increases ductility, but decreases the plateau stress and volumetric energy absorption of ZA27 and its MSFs.
5. At 300°C part of the ZA27 microstructure transitions into the brittle  $\beta$ -phase. This transition is completed at the highest testing temperature 350°C. The brittle phase limits the strength reduction at these temperatures and reintroduces minor plateau stress oscillations.

6. Two different transitions are observed for solid ZA27 and the MSFs. From 25→100°C a brittle to ductile transition occurs. A ductile to quasi-brittle transition is observed in the temperature range 300→350°C.
7. The relative reduction of the 1% offset yield stress with increasing temperature of P-MSF and G-MSF is near identical. Furthermore, it follows closely the trend of solid ZA27. Hence, the foam strength is controlled by the metallic alloy.
8. The relative reduction of the plateau stress and the volumetric energy absorption of P-MSF and G-MSF is similar. However, this reduction is distinctly less than observed for solid ZA27. A possible explanation is the interruption of shear planes by embedded particles.

### Appendix. Physical and mechanical properties of MSF and ZA27 samples

Table 3. Physical properties of foam samples

Sample code	Filler Particle	Mass	Diameter	Height	Density	Testing temperature	$\Phi_{ZA27}$	$\Phi_P$	$\Phi_V$
[-]	[-]	[g]	[mm]	[mm]	[g/cm <sup>3</sup> ]	[°C]	[-]	[-]	[-]
ZP-19	EP	48.10	26.86	41.91	2.026	25	38.71	56.88	4.41
ZP-11		51.04	26.86	43.37	2.076		39.41	56.88	3.71
ZP-14		51.03	26.89	42.56	2.112		40.65	56.88	2.47
ZP-13	EP	48.07	26.86	42.78	1.983	100	37.84	56.88	5.28
ZP-23		48.79	26.84	41.67	2.069		39.56	56.88	3.56
ZP-21		49.60	26.87	41.81	2.092		40.02	56.88	3.10
ZP-22	EP	48.91	26.90	41.83	2.058	200	39.34	56.88	3.78
ZP-12		51.02	26.87	43.13	2.086		39.89	56.88	3.23
ZP-10		52.01	26.89	42.68	2.145		41.07	56.88	2.05
ZP-17	EP	49.03	26.86	43.04	2.011	300	38.40	56.88	4.72
ZP-20		49.37	26.85	42.13	2.069		39.56	56.88	3.56
ZP-16		51.47	26.85	43.38	2.095		40.07	56.88	3.05
ZP-18	EP	49.93	26.86	42.97	2.050	350	39.17	56.88	3.95
ZP-9		50.17	26.90	42.32	2.086		39.90	56.88	3.22
ZP-15		51.81	26.88	42.92	2.128		40.73	56.88	2.39
ZG-23	EG	43.71	26.92	42.69	1.799	25	31.78	61.05	7.17
ZG-15		45.29	26.90	43.14	1.847		32.74	61.05	6.21
ZG-17		45.45	26.88	43.04	1.861		33.02	61.05	5.93
ZG-21	EG	42.44	26.92	42.71	1.746	100	30.71	61.05	8.24
ZG-10		44.95	26.98	42.97	1.830		32.4	61.05	6.55
ZG-20		44.74	26.92	42.37	1.856		32.92	61.05	6.03

ZG-9		44.51	26.95	42.75	1.825		32.30	61.05	6.65
ZG-18	EG	45.28	26.89	42.98	1.855	200	32.90	61.05	6.05
ZG-14		46.55	26.94	43.40	1.882		33.45	61.05	5.50
ZG-12		44.42	26.92	43.57	1.791		31.62	61.05	7.33
ZG-11	EG	45.56	26.90	43.71	1.834	300	32.48	61.05	6.47
ZG-16		45.79	26.91	43.28	1.861		33.01	61.05	5.94
ZG-22		43.99	26.90	42.49	1.822		32.22	61.05	6.73
ZG-13	EG	45.84	26.92	43.60	1.847	350	32.74	61.05	6.21
ZG-19		44.82	26.90	42.23	1.868		33.16	61.05	5.79

Table 4. Mechanical properties of expanded P-MSF samples

Sample code	Testing Temperature	Quasi elastic gradient	0.2% offset yield stress	1% offset yield stress	Plateau stress	Plateau end strain	Energy absorption	Energy absorption efficiency
[-]	[°C]	[MPa]	[MPa]	[MPa]	[MPa]	[%]	[MJ/m <sup>3</sup> ]	[%]
ZP-19	25	4135.20	24.16	56.43	65.45	60.60	31.23	88.58
ZP-11		3868.81	24.37	61.55	67.89	71.03	32.69	87.77
ZP-14		4486.21	30.30	61.93	74.04	63.10	35.54	83.95
ZP-13	100	1673.60	26.92	32.37	56.72	41.44	26.89	56.71
ZP-23		1955.96	28.67	37.26	63.77	41.18	30.37	56.80
ZP-21		1875.54	32.74	39.90	64.26	41.53	30.82	57.17
ZP-22	200	1087.99	15.18	18.70	40.32	40.00	19.10	52.51
ZP-12		1098.13	16.86	20.36	40.54	40.19	19.25	53.82
ZP-10		1325.71	12.66	20.10	42.72	40.69	20.24	53.61
ZP-17	300	718.16	9.16	10.71	26.03	41.07	11.87	53.71
ZP-20		618.60	8.57	10.53	28.02	42.27	12.60	51.75
ZP-16		616.30	7.63	10.18	28.99	41.37	12.94	52.16
ZP-18	350	574.38	8.27	8.91	30.28	43.36	10.30	59.54
ZP-15		570.75	7.25	8.18	30.34	42.08	12.94	55.46

Table 5. Mechanical properties of G-MSF samples

Sample code	Testing Temperature	Quasi elastic gradient	0.2% offset yield stress	1% offset yield stress	Plateau stress	Plateau end strain	Energy absorption	Energy absorption efficiency
[-]	[°C]	[MPa]	[MPa]	[MPa]	[MPa]	[%]	[MJ/m <sup>3</sup> ]	[%]
ZG-23	25	3812.38	28.91	44.38	46.17	63.53	22.18	91.17
ZG-15		3564.27	22.86	49.95	58.10	54.73	27.41	80.83
ZG-17		3803.83	30.37	53.48	58.44	59.61	27.93	81.96
ZG-21	100	1764.19	22.48	26.41	41.23	41.72	20.05	56.81
ZG-10		1867.55	26.80	32.81	48.32	41.44	23.75	56.19
ZG-20		1814.69	29.21	34.40	50.29	41.25	24.63	56.19
ZG-9	200	1086.08	15.56	17.08	30.34	40.73	14.78	52.48
ZG-18		1197.87	15.97	17.94	31.35	40.29	15.39	51.58
ZG-14		1133.36	15.73	17.48	31.81	40.28	15.60	50.64
ZG-12	300	653.56	6.91	8.05	21.11	41.38	9.56	47.99
ZG-11		678.05	9.34	10.15	21.98	40.76	10.16	52.11
ZG-16		713.41	9.19	10.33	24.20	41.90	10.90	51.88
ZG-13	350	582.14	7.09	7.98	26.00	42.52	11.36	55.07
ZG-19		629.67	7.29	7.93	25.30	44.82	10.96	54.31

Table 6. Mechanical properties of solid ZA27 samples

Sample code	Testing Temperature	Quasi elastic gradient	0.2% offset yield stress	1% offset yield stress	Plateau stress	Plateau end strain	Energy absorption	Energy absorption efficiency
[-]	[°C]	[MPa]	[MPa]	[MPa]	[MPa]	[%]	[MJ/m <sup>3</sup> ]	[%]
ZA27-1	25	10478.36	335.30	486.36	624.14	52.46	287.53	78.12
ZA27-2	100	7300.59	251.59	304.88	377.08	46.84	183.86	72.80
ZA27-3	200	5308.11	138.84	170.14	282.28	52.22	129.40	72.77
ZA27-4	300	3463.51	76.02	108.36	185.34	61.90	84.64	81.12
ZA27-5	350	3332.62	59.68	90.87	161.72	70.82	74.97	87.19

## References

- [1] Ashby MF, Evans A, Fleck NA et al. *Metal Foams: A Design Guide*. Butterworth-Heinemann, Oxford, UK, ISBN 0-7506-7219-6, 2000.
- [2] Marsavina L, Kovacic J, Linul E. Experimental validation of micromechanical models for brittle aluminium alloy foam. *Theor Appl Fract Mech* 2016;83:11-18.
- [3] Liang M, Lu F, Zhang G, Li X. Experimental and numerical study of aluminum foam-cored sandwich tubes subjected to internal air blast. *Compos Part B-Eng* 2017;125:134-143.
- [4] Pang X, Du H. Dynamic characteristics of aluminium foams under impact crushing. *Compos Part B-Eng* 2017;112:265-277.
- [5] Pham TM, Chen W, Kingston J, Hao H. Impact response and energy absorption of single phase syntactic foam. *Compos Part B-Eng* 2018;150:226-233.
- [6] Garcia CD, Shahapurkar K, Doddamani M et al. Effect of arctic environment on flexural behavior of fly ash cenosphere reinforced epoxy syntactic foams. *Compos Part B-Eng* 2018;151:265-273.
- [7] Taherishargh M, Vesenjask M, Belova IV et al. In situ manufacturing and mechanical properties of syntactic foam filled tubes. *Mater Des* 2016;99:356-368.
- [8] Shahapurkar K, Garcia CD, Doddamani M et al. Compressive behavior of cenosphere/epoxy syntactic foams in arctic conditions. *Compos Part B-Eng* 2018;135:253-262.
- [9] Linul E, Marsavina L, Kovacic J. Collapse mechanisms of metal foam matrix composites under static and dynamic loading conditions. *Mat Sci Eng A* 2017;690:214-224.
- [10] Berardi VP, Perrella M, Feo L, Cricri G. Creep behavior of GFRP laminates and their phases: Experimental investigation and analytical modeling. *Compos Part B-Eng* 2017;122:136-144.
- [11] Movahedi N, Linul E. Quasi-static compressive behavior of the ex-situ aluminum-alloy foam-filled tubes under elevated temperature conditions. *Mater Lett* 2017;206:182-184.
- [12] Myers K, Katona B, Cortes P, Orbulov IN. Quasi-static and high strain rate response of aluminum matrix syntactic foams under compression. *Compos Part A* 2015;79:82-91.
- [13] Wang L, Limodin N, Bartali A et al. Influence of pores on crack initiation in monotonic tensile and cyclic loadings in lost foam casting A319 alloy by using 3D in-situ analysis. *Mat Sci Eng A* 2016;673:362-372.
- [14] Wu Y, Tang L, Liu Z, Zhang X. Numerical study of the shape irregularity gradient in metallic foams under different impact velocities. *J Mater Eng Perform* 2017;26(8):3892-3900.

- [15] Szlancsik A, Katona B, Májlinger K, Orbulov IN. Compressive behavior and microstructural characteristics of iron hollow sphere filled aluminum matrix syntactic foams. *Materials* 2015;8:7926-7937.
- [16] Gibson LJ, Ashby MF. *Cellular solids: structure and properties*. Cambridge: Cambridge University Press, UK, 1997.
- [17] Taherishargh M, Belova IV, Murch GE, Fiedler T. Low-density expanded perlite–aluminium syntactic foam. *Mat Sci Eng A* 2014;604:127-134.
- [18] Borovinšek M, Taherishargh M, Vesenjāk M, Ren Z, Fiedler T. Geometrical characterization of perlite-metal syntactic foam. *Mater Charact* 2016;119:209-215.
- [19] Peroni L, Scapin M, Fichera C. et al. Investigation of the mechanical behaviour of AISI 316L stainless steel syntactic foams at different strain-rates. *Compos Part B* 2014;66:430-442.
- [20] Taherishargh M, Belova IV, Murch GE, Fiedler T. On the mechanical properties of heat-treated expanded perlite-aluminium syntactic foam. *Mater Des* 2014;63:375-383.
- [21] Taherishargh M, Belova IV, Murch GE, Fiedler T. The effect of particle shape on mechanical properties of perlite/metal syntactic foam. *J Alloys Compd* 2017;693:55-60.
- [22] Taherishargh M, Sulong MA, Belova IV, Murch GE, Fiedler T. On the particle size effect in expanded perlite aluminium syntactic foam. *Mater Des* 2015;66:294-303.
- [23] Orbulov IN. Compressive properties of aluminium matrix syntactic foams. *Mat Sci Eng A* 2012;555:52-56.
- [24] Broxtermann S, Taherishargh M, Belova IV et al. On the compressive behaviour of high porosity expanded Perlite-Metal Syntactic Foam (P-MSF). *J Alloys Compd* 2017;691:690-697.
- [25] Taherishargh M, Linul E, Broxtermann S, Fiedler T. The mechanical properties of expanded perlite-aluminium syntactic foam at elevated temperatures. *J Alloys Compd* 2018;737:590-596.
- [26] Fiedler T, Taherishargh M, Krstulović-Opara L, Vesenjāk M. Dynamic compressive loading of expanded perlite/aluminium syntactic foam. *Mat Sci Eng A* 2015;626:296-304.
- [27] Luong DD, Shunmugasamy VC, Gupta N et al. Quasi-static and high strain rates compressive response of iron and Invar matrix syntactic foams. *Mater Des* 2015;66:516-531.
- [28] Fiedler T, Belova IV, Murch GE. On the thermal properties of expanded perlite – Metallic syntactic foam. *Int J Heat Mass Tran* 2015;90:1009-1014.
- [29] Kádár C, Máthis K, Orbulov IN, Chmelík F. Monitoring the failure mechanisms in metal matrix syntactic foams during compression by acoustic emission. *Mater Lett* 2016;173:31-34.

- [30] Al-Sahlani K, Broxtermann S, Lell D, Fiedler T. Effects of particle size on the microstructure and mechanical properties of expanded glass-metal syntactic foams. *Mat Sci Eng A* 2018;728:80-87.
- [31] Al-Sahlani K, Taherishargh M, Kisi E, Fiedler T. Controlled shrinkage of expanded glass particles in metal syntactic foams. *Materials* 2017;10(9):1073.
- [32] Sahu S, Goel MD, Mondal DP, Das S. High temperature compressive deformation behavior of ZA27–SiC foam. *Mater Sci Eng A* 2014;607:162-172.
- [33] Linul E, Movahedi N, Marsavina L. The temperature and anisotropy effect on compressive behavior of cylindrical closed-cell aluminum-alloy foams. *J Alloys Compd* 2018;740:1172-1179.
- [34] ASTM B86- 13. Standard Specification for Zinc and Zinc-Aluminum (ZA) Alloy Foundry and Die Castings.
- [35] <https://www.makeitfrom.com/material-properties/Sand-Cast-Zinc-Aluminum-27>.
- [36] Liu Y, Li HY, Jiang HF, Lu XC. Effects of heat treatment on microstructure and mechanical properties of ZA27 alloy. *Trans Nonferrous Met Soc China* 2013;23(3):642-649.
- [37] Bobic B, Bajat J, Acimovic-Pavlovic Z, Rakin M, Bobic I. The effect of T4 heat treatment on the microstructure and corrosion behaviour of Z227A11.5Cu0.02Mg alloy. *Corros Sci* 2011;53:409-417.
- [38] Miroslva B, Vencl A, Mitrovic S, Bobic I. Influence of T4 heat treatment on tribological behavior of ZA27 alloy under lubricated sliding condition. *Tribol Lett* 2009;36:125-134.
- [39] Allameh-Haery H, Kisi E, Pineda J, Suwal LP, Fiedler T. Elastic properties of green expanded perlite particle compacts. *Powder Technol* 2017;310:329-342.
- [40] Movahedi N, Linul E, Marsavina L. The temperature effect on the compressive behavior of closed-cell aluminum-alloy foams. *J Mater Eng Perform* 2018;27(1):99-108.
- [41] Ares AE, Gassa LM. Corrosion susceptibility of Zn–Al alloys with different grains and dendritic microstructures in NaCl solutions. *Corros Sci* 2012;59:290-306.
- [42] ISO13314. Mechanical testing of metals - Ductility testing - Compression test for porous and cellular metals, Switzerland, 2011.
- [43] Linul E, Marsavina L, Kovacic J, Sadowski T. Dynamic and quasi-static compression tests of closed-cell aluminium alloy foams. *P Romanian Acad A* 2017;18(4):361-369.
- [44] Daoud A. Synthesis and characterization of novel ZnAl22 syntactic foam composites via casting. *Mater Sci Eng A* 2008;488:281-295.

- [45] Al-Sahlani K, Broxtermann S, Lell D, Fiedler T. Effect of particle size on the microstructure and mechanical properties of expanded glass-metal syntactic foams. *Mat Sci Eng A* 2018;728:80-87.
- [46] Venkatappa S, Sharma KV. Influence of heat treatment on microstructure and mechanical properties of some zinc based alloys. *IJoMS* 2011;6:57-64.
- [47] Prasad B. Microstructure and tensile property characterization of a nickel-containing zinc-based alloy: effects of heat treatment and test conditions. *Mater Sci Eng A* 2000;277:95-101.
- [48] Huang K, Logé RE. A review of dynamic recrystallization phenomena in metallic materials. *Mater Des* 2016;111:548-574.
- [49] Sahu S, Goel MD, Mondal DP, Das S. High temperature compressive deformation behavior of ZA27–SiC foam. *Mat Sci Eng A* 2014;607:162-172.
- [50] Li HY, Liu Y, Lu XC, Su XJ. Constitutive modeling for hot deformation behavior of ZA27 alloy. *J Mater Sci* 2012;47:5411-5418.
- [51] Linul E, Şerban DA, Marsavina L, Kovacic J. Low-cycle fatigue behaviour of ductile closed-cell aluminium alloy foams. *Fatig Fract Eng Mater Struct* 2017;40(4):597-604.
- [52] Szlancsik A, Katona B, Bobor K et al. Compressive behaviour of aluminium matrix syntactic foams reinforced by iron hollow spheres. *Mater Des* 2015;83:230-237.
- [53] Kumaraswamidhas LA, Rajak DK, Das S. An investigation on axial deformation behavior of thin-wall unfilled and filled tube with aluminum alloy (Al-Si7Mg) foam reinforced with SiC particles. *J Mater Eng Perform* 2016;25(8):3430-3438.
- [54] Linul E, Movahedi N, Marsavina L. On the lateral compressive behavior of empty and ex-situ aluminum foam-filled tubes at high temperature. *Materials* 2018;11(4):554.
- [55] Linul E, Movahedi N, Marsavina L. The temperature effect on the axial quasi-static compressive behavior of ex-situ aluminum foam-filled tubes. *Compos Struct* 2017;180:709-722.
- [56] Kováčik J, Jerz J, Mináriková N et al. Scaling of compression strength in disordered solids: metallic foams. *Frattura ed Integrita Strutturale* 2016;36:55-62.
- [57] Kováčik J, Orovčík L, Jerz J. High-temperature compression of closed cell aluminium foams. *Kovove Mater* 2016;54(6):429-441.

## Figure Captions

**Fig. 1.** Samples: P-MSF (left), solid ZA27 (center), and G-MSF (right)

**Fig. 2.** Solid ZA27: (a) compressive stress-strain data, (b) magnified stress-strain curves, (c) deformation sequence at 25°C

**Fig. 3.** Microstructure of ZA27 alloy before compression tests (a); Isometric (b), top (c) and lateral (d) view of deformed solid ZA27 samples; sample cross-section (e) and microstructure of deformed samples (f) at different testing temperatures

**Fig. 4.** Mechanical characteristics of solid ZA27 samples at different temperatures: (a) stresses, (b) energy absorption and plateau end strain

**Fig. 5.** Compression of P-MSFs and G-MSFs at different temperatures: (a) stress-strain data, (b) deformation sequence at 25°C.

**Fig. 6.** Deformed P-MSFs (a) and G-MSFs (c) samples after different testing temperatures, and optical images (b, d) of the outer sample surfaces (magnification 8x)

**Fig. 7.** Cross-sections of deformed MSF: (a, d) photographs, (b, e) stereographic view (8x magnification), (c, f) SEM images

**Fig. 8.** Mechanical properties of P-MSF and G-MSF: (a) quasi-elastic modulus, (b) 1.0% offset yield stress, (c) plateau end strain / plateau stress, (d) energy absorption

**Fig. 9.** Reduction percentage of quasi-elastic modulus (a), 1% offset yield stresses (b), plateau stress (c) and energy absorption (d) for MSFs and solid ZA27 samples at different temperatures normalized by 25°C values

## Table Captions

**Table 1.** Chemical composition of ZA27 alloy [35]

**Table 2.** Testing temperatures and ZA27 phases

**Table 3.** Physical properties of foam samples

**Table 4.** Mechanical properties of expanded P-MSF samples

**Table 5.** Mechanical properties of G-MSF samples

**Table 6.** Mechanical properties of solid ZA27 samples